

This is a Preprint that has received USGS Bureau Approval for publication. This is version 1 of this Preprint, submitted to the journal Earth and Space Science for peer review

Authors:

Daniel Buscombe,

Marda Science LLC, contracted to USGS Pacific Coastal and Marine Science Center, CA.

Email: dbuscombe@contractor.usgs.gov

Twitter: @magic_walnut

Evan B. Goldstein,

Department of Geography, Environment, and Sustainability, University of North Carolina at Greensboro, Greensboro, North Carolina, USA.

Email: ebgoldst@uncg.edu

Twitter: @ebgoldstein

A Reproducible and Reusable Pipeline for Segmentation of Geoscientific Imagery

D. Buscombe¹, E. B. Goldstein²

¹Marda Science, LLC, contracted to USGS Pacific Coastal and Marine Science Center, Santa Cruz,
California, USA.

²Department of Geography, Environment, and Sustainability, University of North Carolina at Greensboro,
Greensboro, North Carolina, USA.

Key Points:

- We develop software for segmentation of geoscientific imagery with fully convolutional deep neural network models.
- The software presents options for users, but relies on a reusable template that allows for rapid experimentation.
- We demonstrate an example workflow with Landsat 8 imagery, and compare loss functions, model size, and model architectures.

Abstract

Segmentation of Earth science imagery is an increasingly common task. Among modern techniques that use Deep Learning, the UNet architecture has been shown to be a reliable for segmenting a range of imagery. We developed software - Segmentation Gym - to implement a data-model pipeline for segmentation of scientific imagery using a family of UNet models. With an existing set of imagery and labels, the software uses a single configuration file that handles dataset creation, as well as model setup and model training. Key benefits of this software are a) the focus on reproducible dataset creation and modeling, and b) the ability for quick model experimentation through changes to a configuration file. Quick experimentation permits researchers to prototype different model architectures, sizes, and adjust common hyperparameters to find a suitable model. We demonstrate the use of the software using a dataset of 419 labeled Landsat-8 scenes of coastal environments and compare results across two model architectures, five model sizes, and three loss functions. This demonstration highlights that our software enables rapid, reproducible experimentation to determine optimal hyperparameters for specific datasets and research questions.

Plain Language Summary

A common task for Earth scientists is to divide a satellite or aerial image into specific classes. For example, an image of the coastline might be assigned certain pixels as being water, beach, and land. In the Deep Learning world, this is called segmentation. We wrote a piece of software that helps researchers train Deep Learning models to do segmentation on all types of imagery. A major problem with making Deep Learning models is dealing with all the choices on which model to use and quickly testing many options. We have designed our code in such a way that it can easily be adjusted, and will work in many applications and for many common types of Earth science image datasets.

1 Introduction

Image segmentation has become an increasingly important tool in Earth science research (Yuan et al., 2021; Pally & Samadi, 2022; Sun et al., 2022). In recent years, Deep Learning (LeCun et al., 2015) models based on the UNet (Ronneberger et al., 2015) and the Residual UNet (Zhang et al., 2018; Liu et al., 2019) have become the standard in state-of-the-art Earth science applications involving image segmentation (Kattenborn et al., 2019; Nalepa et al., 2019; Liu et al., 2019; Collins et al., 2020; Chen et al., 2020; Hoerer & Kuenzer, 2020; Marangio et al., 2020; Song et al., 2020; Sáez et al., 2021; Xiao et al., 2021; Nagi et al., 2021; Kotaridis & Lazaridou, 2021; Gupta et al., 2021; Verma et al., 2021; van der Meij et al., 2021; Jin et al., 2022; Li et al., 2022; Rafique et al., 2022).

Deep-Learning-based image segmentation (or ‘semantic segmentation’) starts with a research question and relevant labeled training data, i.e., pairs of images and corresponding labels. Training data can come from existing sources (e.g., Wernette et al., 2022) or made from scratch using labeling tools (e.g., Buscombe et al., 2021). With training data in hand, researchers are left to wrangle, preprocess and format data, followed by building, training, and evaluating models using one of several Deep Learning frameworks. This work often requires substantial trial-and-error experimentation; choosing a model and training technique, as well as implementing those techniques, can be challenging (Yuan et al., 2021). Further, guidance in published papers and code repositories often only present the author’s best model (in terms of a validation metric), and not the extensive model training trials that might inform other experiments for a researcher to try when developing a suitable model. This points to a gap in the current software landscape, namely an end-to-end pipeline for geoscientific image segmentation that makes quick experimentation relatively easy.

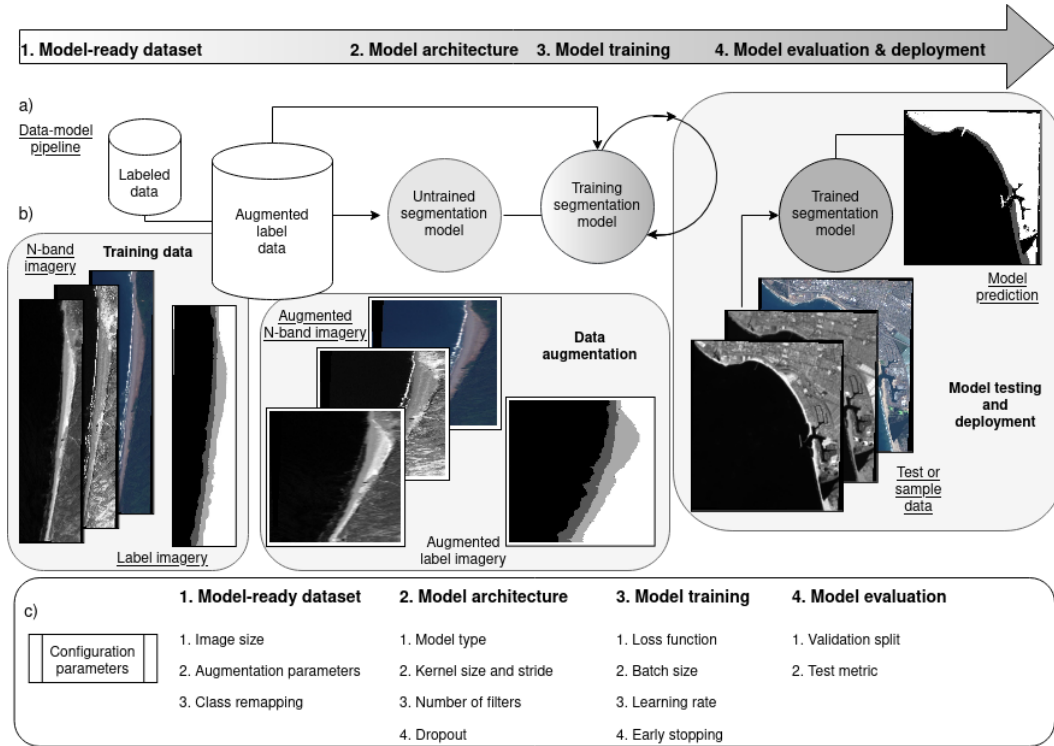


Figure 1. Schematic diagram of the data-model pipeline (a) encoded in the Segmentation Gym software, with examples of model inputs and outputs (b). The four basic pipeline stages are depicted (from left to right): 1. model-ready dataset creation; 2. model architecture (model building); 3. model training; and 4. model evaluation, each with their own set of configuration settings that govern behavior (c).

To fill this gap and aid in the adoption and use of Deep Learning image segmentation, we developed software named ‘Segmentation Gym’ to allow researchers to quickly implement and experiment with segmentation with their own imagery. A fully reproducible workflow enables users to adjust a configuration file and perform their own experimentation with hyperparameters. Segmentation Gym enables its users to fully document the computational provenance of their data models using openly accessible and citable methods (Gil et al., 2016), which moves Earth science segmentation practices closer to realizing a goal of being fully reproducible (Donoho, 2010).

In addition to presenting the design of Segmentation Gym, we demonstrate its use with an example using a dataset consisting of 419 image-label pairs. The labeled imagery consist of Landsat-8 scenes of coastal environments from a large collection of labeled images (Wernette et al., 2022; Buscombe et al., 2022). We examine the sensitivity of model outputs to hyperparameter choices that govern model architecture and training strategies. We compare two Deep Learning model architectures (UNets and Residual UNets), five different model sizes, and three different loss functions. The goal of this demonstration is to highlight how researchers can draw insight from the results of this experiment, and adapt a similar modeling campaign with their own data.

2 Implementation

2.1 Overview

We outline the implementation of the software (Figure 1) below in five sections. First, we describe the routines to create a model-ready dataset, which ingest data, merge data bands from files, augment the data, remap classes on-the-fly (if necessary), and format it into batches of tensors of a certain size for model training. Second, we describe the model building process, which involves experimenting with model architecture, such as how large and how numerous feature-extracting kernels are, and experimenting with the use of regularizing layers. Third, model training is described. Fourth, we discuss model evaluation routines, requiring the use of metrics to quantify accuracy on a hold-out dataset. Training often involves experimenting with hyperparameters such as the loss function and learning rate. Therefore lastly, we describe how model reproducibility is ensured, for example by using the same training and validation examples for successive experimentation, such as to test the outcome of retraining with new hyperparameters.

The Python software (Buscombe & Goldstein, 2022) relies on Numpy (Harris et al., 2020), Tensorflow (Abadi et al., 2015), and Keras (Chollet et al., 2015; Chollet, 2021), and is designed to run in an isolated conda (Conda, 2022) environment, a cross-platform and open-source package management system. Models are typically trained using GPUs but a CPU may also be used.

Training a segmentation model requires image-label pairs, and users come to this segmentation workflow with a folder of images and a folder of corresponding labels. Segmentation Gym is part of an ecosystem of tools that includes the labeling program ‘Doodler,’ described by Buscombe et al. (2021). Images labeled using Doodler are readily ingested into the model pipeline (Figure 1), but label images acquired by other means are also supported.

The components outlined in Figure 1 permit rapid exploratory modeling, which is necessary because determining a successful model implementation often can take experimentation. A single configuration file (Figure 1) controls all of the data creation and model training hyperparameters, such as input data size, on-the-fly class remapping, data augmentation behavior, training hyperparameters, regularization, model loss, and model architecture. Configuration files are JSON files containing a data-model pipeline recipe encoded as variables and their values. Therefore each model building trial may be documented by the configuration file that made it.

2.2 Model-ready dataset creation

The routine to convert image-label pairs into formats amenable for training a model is opinionated (Parker, 2017; Ostblom & Timbers, 2021; Peng & Parker, 2021). For example, by design we force users into a certain way of preparing data. In return, users have their data batched and preprocessed in a way that we have found to be successful for training segmentation models using a range of geoscientific imagery.

First, the user is prompted via a Graphical User Interface (GUI) to enter the path to the images, labels, and a place to store the output files. Imagery can consist of 1 or more bands in 8-bit unsigned formats. The program allows either a) 3-band imagery, such as most visible-band photographic data; b) 1-band imagery, such as other spectral and hyperspectral bands or indices, or bespoke geophysical data bands; or c) merging of 1- or 3-band imagery with any number of additional 1-band images that are coincident in space.

Second, images are standardized by subtracting the mean and dividing by the standard deviation. This is a crucial step towards good model performance on sample imagery whose distributions may differ from the imagery used to train the model (Yuan

130 et al., 2021; Li et al., 2022). Standardizing imagery diminishes the importance of out-
131 lier distributions of image values, ensuring better transferability from training to sam-
132 ple imagery.

133 Third, both images and labels are resized to the target dimensions, and also zero-
134 padded if necessary. Fully convolutional models expect input imagery to all be the same
135 specified size, and it is common practice to resize and reshape imagery to a desired tar-
136 get dimensions. Zero-padding involves placing an image in the center of a large matrix
137 of zeros, such that the boundary pixels of the resulting image are all zero (with a cor-
138 responding zero-valued label integer to denote a null class). Padding is necessarily car-
139 ried out on imagery that has a range of dimensions; if the imagery is smaller than the
140 target dimensions, it is zero-padded. If, however, the imagery is larger than the target
141 dimensions, it is first shrunk (i.e., resampled to a coarser spatial dimension), then zero-
142 padded.

143 Fourth, classes in the labeled imagery can optionally be remapped. Datasets for
144 image segmentation come with labels from pre-determined class sets. Those classes may
145 be merged, split or otherwise remapped from one set of classes to another, depending
146 on the intended application. For example, if the integer 1 is used to encode the class la-
147 bel ‘ocean,’ and the integer 2 is used to denote ‘river,’ those two classes might be merged
148 such that integers 1 and 2 both denote a third common class, ‘water.’ Remapped label
149 imagery is stored directly in the output files.

150 Finally, data undergo augmentation. Augmentation creates transformed versions
151 of the data (Stivaktakis et al., 2019; van Lieshout et al., 2020; Rafique et al., 2022) and
152 is carried out by means of the standard operations available in Keras, such as rotation,
153 width and height shift, zoom, and vertical and horizontal flips. The primary purpose is
154 regularization; by providing alternative versions of the data, the model learns feature rep-
155 resentations that are invariant to location, scale, translation, etc. Using augmented im-
156 agery to train a model permits oversampling (increasing the size of a dataset) without
157 excessive redundancy, because all oversampled augmented imagery will have unique, ran-
158 dom augmentations. Optionally, augmentation may be disabled, in which case non-augmented
159 data are used. Examples of augmented and non-augmented images with labels overlaid
160 are printed to file for visual verification.

161 The model training pipeline stores image/label pairs as a TensorFlow Dataset. This
162 format allows for convenient batching, shuffling, and loading of the dataset during model
163 training and evaluation. The model training pipeline takes advantage of the TensorFlow
164 Data Application Programming Interface (API) (*Tensorflow datasets*, 2022), which rep-
165 resents a sequence of single training example, with a pair of tensor components repre-
166 senting the image and its label. Each image and its corresponding label are stored in the
167 compressed numpy binary format, npz (also used by Doodler) as a sequence of binary
168 strings, which allow large datasets to be sequentially loaded to the local (GPU or CPU)
169 memory during model training and evaluation.

170 **2.3 Model building**

171 Currently, Segmentation Gym implements types of UNet and Residual UNet mod-
172 els. A UNet (Ronneberger et al., 2015) today generally refers to a family of models iden-
173 tified by the following characteristics (Figure 2): a) fully convolutional (no fully connected
174 layers); b) four convolutional ‘blocks’ consisting of convolutional layers and Batch Nor-
175 malization layers connected by ReLu activations, then optionally, Dropout layers; and
176 c) symmetrical U shape (hence the ‘U’ in the name) with skip connections encoding the
177 Encoder and Decoder branches (Figure 2). Specific UNet implementations often differ
178 in a) number of filters, b) stride length (i.e., feature extraction specifics), c) use of (and
179 type and relative location of) Dropout.

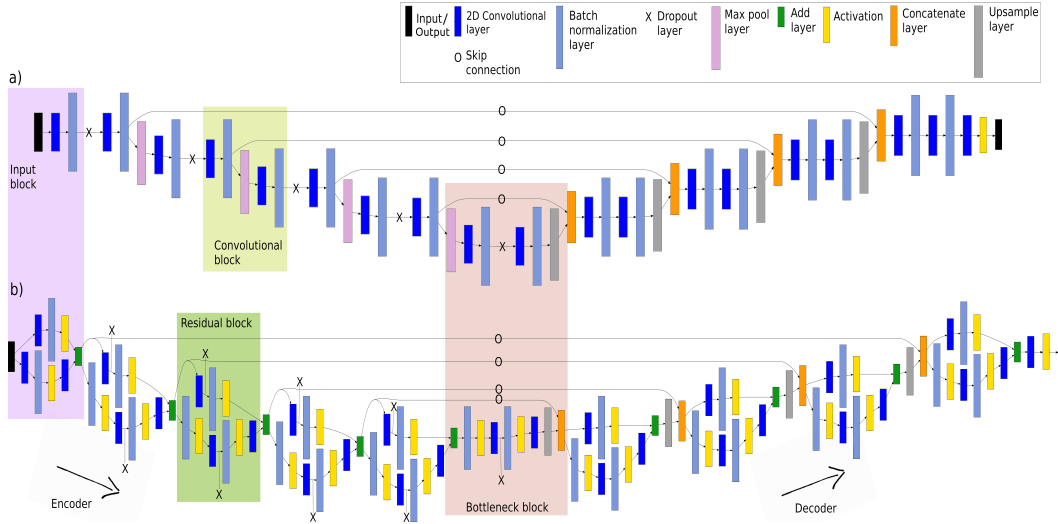


Figure 2. The a) UNet and b) Res-UNet fully convolutional model architectures used in the present study. There are several forms of these models available in the software ‘Segmentation Gym’.

180 Our UNet (Figure 2A) and Res-UNet (Figure 2B) architecture implementations
 181 differ only through the use of residual connections in convolutional blocks in the latter.
 182 Residual connections add the outputs of the regular convolutional block with the inputs,
 183 so the model learns to map feature representations in context to the inputs that created
 184 those representations (Drozdal et al., 2016). Residual connections (Drozdal et al., 2016)
 185 have been shown in numerous contexts to facilitate information flow during model train-
 186 ing (Zhang et al., 2018; Liu et al., 2019; Nagi et al., 2021).

187 The Encoder branch (Figure 2) receives the input image and applies a series of Con-
 188 volutional and Batch Normalization layers, and optionally Dropout layers, followed by
 189 Pooling layers that reduce the spatial size and condense features. Four banks of convo-
 190 lutional filters each use filters that double in size to the previous, thereby progressively
 191 downsampling the inputs as features are extracted through pooling. The last set of fea-
 192 tures (or so-called bottleneck) is a very low-dimensional feature representation of the in-
 193 put imagery. The Decoder upsamples the bottleneck into a label image progressively us-
 194 ing convolutional filters, each using filters half in size to the previous, thereby progres-
 195 sively upsampling the inputs as features are extracted through transpose convolutions
 196 and concatenation. The sets of features from each of the four levels in the Encoder-Decoder
 197 structure are concatenated, which allows learning different features at different levels and
 198 leads to spatially well-resolved outputs. The final classification layer maps the output
 199 of the previous layer to a single 2D output based on a Sigmoid activation function.

200 2.4 Model training

201 The routine for training a model is opinionated through the specification of the num-
 202 erical optimizer that guides training, and through the use of a deterministic learning
 203 rate scheduler. Neural networks are trained with variations of the stochastic gradient de-
 204 scent (SGD) algorithm, and the specific form of numerical optimizer is a hyperparam-
 205 eter. We use the Adam optimizer (Kingma & Ba, 2014), a variation of SGD. Schmidt
 206 et al. (2020) found Adam to be a good choice for almost all Deep Learning models based
 207 on Convolutional layers. Other important model training variables specified in the con-
 208 figuration file are a) batch size, b) loss function, and c) learning rate. These tend to have

209 a greater impact on final model accuracy than other tunable hyperparameters such as
 210 kernel size, number of convolutional filters, and Dropout, and are therefore described in
 211 more detail below.

212 Datasets are typically larger than can be held in memory so models are trained in
 213 batches. Batch size can be an important hyperparameter; when the model is presented
 214 with a batch of, say, six images, and six corresponding labels, the model performance
 215 and the magnitude of weight adjustment during backpropagation will be evaluated as
 216 the average of the six individual discrepancies between model predictions and ground-
 217 truth labels. Therefore the size of the batch has an effect on the model's ability to rec-
 218 ognize patterns in the presence of variability, with larger variability given by large batch
 219 sizes, and hence its rate of convergence in training. Where possible, we recommend us-
 220 ing the largest batch size your available GPU memory will allow. Larger batch sizes tend
 221 to promote more stable validation loss curves. This is usually only possible with rela-
 222 tively large hardware, because large batches mean larger amounts of GPU memory re-
 223 quired. You may therefore decide to use a smaller model input size to achieve a larger
 224 batch size if necessary.

225 During training, the distribution of accuracy scores over classes are optimized us-
 226 ing a loss function. Segmentation Gym provides various options for loss function. In this
 227 contribution we compare three loss functions, namely mean Dice, categorical cross-entropy
 228 or CCE, and Kullback-Leibler distance or KLD. The mean Dice coefficient is given by
 229 $D = 2|Y \cap \hat{Y}| / (|Y| + |\hat{Y}|)$, where Y and \hat{Y} are true and estimated label images, respec-
 230 tively, \cap is intersection. Mean Dice is a spatial metric that is relatively insensitive to class-
 231 imbalance, or the tendency for a majority class to dominate over one or more minority
 232 classes (Csurka et al., 2004). This is because the numerator is the number of correctly
 233 classified pixels, and the denominator is the total number of pixels in a class that is in
 234 both estimated and ground truth. We therefore can use $1 - D$ as a loss function dur-
 235 ing class-imbalanced model training, and D to evaluate model results. Many geoscience
 236 datasets are significantly imbalanced, and rare classes may be scientifically important,
 237 therefore a loss function such as $1 - D$ that handles this can be important for model ac-
 238 curacy. Categorical cross-entropy, $C = -\sum_c Y \log(\hat{Y})$, is a measure of the difference
 239 between two distributions over a class set, c , i.e., the target or ground truth and the cur-
 240 rent model estimate, and is a generalization of log loss to multi-class classification prob-
 241 lems. Kullback-Leibler distance measures divergence in class-probability distributions
 242 and is given by $KLD = \sum_c Y \log(Y/\hat{Y})$.

243 We vary the learning rate deterministically using a scheduler function that assigns
 244 a specific learning rate value as a function of model training epoch. A model epoch is
 245 a full training pass over the entire dataset such that each example has been seen once.
 246 Thus, an epoch represents $N/\text{batch size}$ training iterations, where N is the total num-
 247 ber of examples in the training set. We make use of a function that starts with a small
 248 learning rate, then quickly ramps up to a maximum, then decays exponentially. An ad-
 249 vantage of varying the learning rate deterministically using a scheduler is to make train-
 250 ing reproducible. Decaying the learning rate as training progresses allows the model to
 251 slowly converge on an optimal solution. This procedure prevents the solution from get-
 252 ting stuck in a so-called 'saddle point,' which is a local minimum much higher than the
 253 global minimum. Without varying the learning rate, large updates to the model can po-
 254 tentially lead to suboptimal convergence or prematurely trigger early stopping criteria.
 255 In addition to a scheduler, we also implement an early stopping criterion, where the model
 256 ceases training early when no improvement to validation loss is observed over a user-defined
 257 number of training epochs. Even when models do end after a differing numbers of epochs,
 258 the scheduler ensures the learning rate varied in the same way for each model.

2.5 Model evaluation

Mean Intersection over Union, given by $IoU = |Y \cap \hat{Y}| / (|Y| + |\hat{Y}| - |Y \cap \hat{Y}|)$, is the canonical metric to evaluate model performance. It is sometimes useful to keep track of multiple metrics (Buscombe et al., 2021). Whereas mean IoU is a spatial measure, *KLD* measures the difference in observed and estimated class-probability distributions. *KLD* is used as an alternative metric. The only variable related to model evaluation specified in the configuration file is the validation split, which is the proportion of all data to use for model validation. The remainder will be used to train the model. Starting with a relatively high validation split should be a goal, to avoid overfitting and promote generalization. If the model is under-performing on the training data, the validation split should be reduced by small increments accordingly.

2.6 Reproducibility

The data creation and model training process in Segmentation Gym is reproducible. We take several steps to enable this reproducibility. First, we use a seed value to instantiate any numerical operations that involved random numbers, and operating system environment variables are used to guarantee reproducibility in some of the software routines that accelerate computation on GPUs. These collectively ensure consistency in dataset creation and in model training. Second, we have adopted the practice of varying the learning rate deterministically using a scheduler function that assigns a specific learning rate value as a function of model training epoch, rather than an adaptive learning rate.

3 Case study

We provide a case study to demonstrate the use of Segmentation Gym, the results obtained from the software, and the experimentation that the software permits. In this example, our goal is to develop a segmentation model that is able to operate on 419 coastal images from Landsat-8 and classify pixels into 1 of 4 classes: water, whitewater, sand, and other. Our specific target is to develop a segmentation model with acceptable accuracy metrics on a relatively large validation subset, without overfitting to the data, that converges to a solution relatively quickly, and is also parsimonious (with only enough parameters to achieve a desired accuracy threshold).

To develop this model we designed an experimental matrix to independently examine the effects on model performance of the following: a) five different numbers of model parameters, b) three alternative loss functions, and c) the presence/absence of residual connections. We kept track of mean IoU and KLD on training and validation portions during model training, and computed those quantities of the validation subset comprising of a reproducibly random draw of 60% of the data and the remainder for model training. The same validation and training data were used to train each model to ensure repeatability and comparison. We also kept track of the epoch at which training was terminated, to quantify model convergence time.

3.1 Data

The labeled imagery we use in the present contribution are one of the ten data records that comprise the Coast Train dataset (Wernette et al., 2022; Buscombe et al., 2022), specifically 419 Landsat-8 (top-of-atmosphere) images and associated labels consisting of time-series from seven coastal locations around the United States (Figure 3a). The dataset consist of visible-band (RGB) imagery, and 2D integer label masks (Figure 3b). The imagery was pre-processed for use in model training. The original 11-classes were remapped into 4 classes: water, whitewater, sand, and other. Images and corresponding label images were zero-padded to 512x512 pixels if smaller than that dimension, and downsized to 512x512 pixels. We also retrieved the Near Infra-Red (NIR) and Short-wave

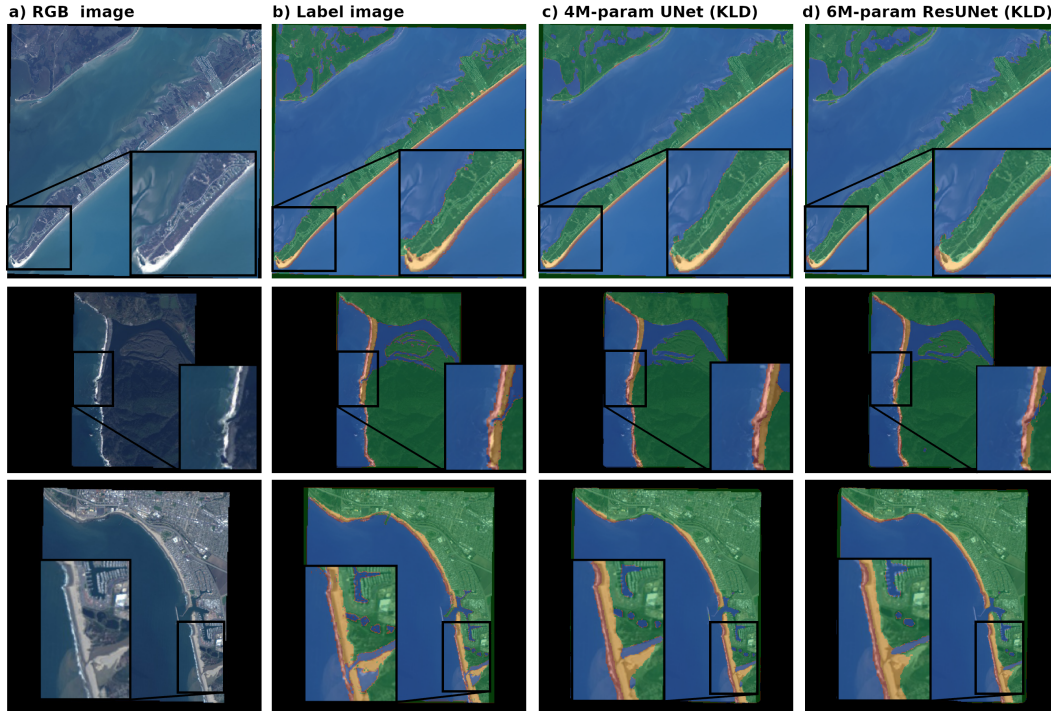


Figure 3. Example model inputs and outputs: a) RGB imagery, b) Label imagery (created using Doodler), c) 4M-parameter UNet model output, d) 6M-parameter Res-UNet model output. In b) through d), labels are shown as colored semi-transparent overlays of the underlying image. Blue indicates water, red is whitewater, yellow is sediment, and green is other. Smaller inset regions are scaled at 200% and better illustrate variability among model outputs, and between model outputs and input label images, as well as error in inputs.

307 Infrared (SWIR) bands associated with each RGB image, because spectral indices that
 308 contain the NIR and especially the SWIR band have been shown to facilitate more re-
 309 liable automated classification of water bodies in coastal regions (Luijendijk et al., 2018;
 310 Vos et al., 2019). We therefore stacked the three-band visible (RGB) 15-m pan-sharpened
 311 imagery with the coincident 15-m pan-sharpened SWIR and NIR bands, and the result-
 312 ing 5-band raster was used as the model training input.

313 3.2 Implementation

314 Images and labels were augmented such that five copies were made each consist-
 315 ing of the original images modified by applying random zoom (up to 5%), rotation (up
 316 to 5%), width and height shifts (up to 5%) and horizontal flips. This resulted in 2095
 317 augmented image-label pairs for model training.

318 We trained 30 different models on the same augmented dataset: 15 UNets and 15
 319 ResUNets. Each 15 consist of five model sizes (in terms of parameters), and 3 loss func-
 320 tions, namely CCE, Dice, and KLD. The number of parameters was varied by adjust-
 321 ing the number of convolutional filters (2,4,6,8, or 12) in the initial convolutional block.
 322 The number of filters doubles every subsequent block on the downsampling (Encoder)
 323 layer, then halves on every subsequent block on the upsampling (Decoder) layer (Fig-
 324 ure 2). Overfitting is countered by three main model regularization strategies, namely
 325 the use of a relatively large validation subset, the use of early stopping, whereby the weights

with the smallest validation loss are stored, not from the last training epoch, and the use of Dropout. We used a Dropout rate of 0.1 on each downsample layer but not on up-sample layers. We use a 7x7 kernel with a stride of 2. Each model was trained with the same learning rate scheduler (varying learning between 1e-7 and 1e-4 based on epoch), and batch size (8). Model training stopped early when the validation loss didn't improve upon its previous best value for 10 epochs. As explained above, all of these parameters are specified in a single configuration file. We therefore trained our 30 models using 30 different configuration files.

3.3 Results

To compare the 30 models, we evaluate mean IoU and KLD for the validation subset. Performance statistics (Figure 4) reveal that Res-UNets tend to outperform UNets, as evidenced by a higher average IoU (Figure 4a-c), lower average KLD (Figure 4d-f), and also a larger accuracy for smaller number of model parameters. The largest discrepancy between Res-UNet and UNet, and highest model accuracy, is observed when CCE is used for loss (Figure 4b). The performance of Res-UNets demonstrate that residual connections improve statistical measures of success, which is corroborated by visual inspection revealing more realistic model outputs.

In these experiments the best loss is CCE, which promotes the fastest convergence, and highest average and maximum IoU scores. Dice is the worst loss in these trials, as evidenced by very long convergences, and lowest scores. Also, IoU scores do not always appreciably increase with increasing model parameters (Figure 4a). All models improve with more parameters, then plateau or even decline in accuracy (Figure 4b,c); an average model size is best overall. Peak Res-UNet model performance tends to occur with fewer parameters compared to an equivalent U-Net.

KLD is a useful model comparative (Figure 4d-f). It reveals similar (inverse) trends to mean IoU, but larger differences between UNet and Res-UNet trained with Dice loss (Figure 4d), smaller differences between UNet and Res-UNet trained with CCE loss (Figure 4e), and IoU and KLD are most similar when KLD loss is used to train a model (Figure 4f). To provide a representative indication of the variation in accuracies per-site, validation Dice coefficients for the mid-sized model trained using CCE were as follows: Duck: $D=.83$ (N=76), Galveston-East: $D=.93$ (N=40), Galveston-West: $D=.94$ (N=40), Klamath: $D=.87$ (N=124), Klamath region: $D=.88$ (N=69), Ocean Beach: $D=.92$ (N=53), Sunset: $D=.90$ (N=46), Ventura: $D=.88$ (N=40). These statistics show that the model performs approximately as well across all areas.

4 Discussion

Deep Learning is a powerful set of tools to develop models to segment imagery because of the lack of restrictions imposed on the input variables (such as their distributions or covariance structure). Despite the rapid pace of Deep Learning research, UNets are likely to continue to have considerable application for a number of reasons. First, their success has been demonstrated across many domains and tasks and are already widely known and effectively used in a wide range of scientific applications. Second, they converge well in training even with relatively small amounts of data. Third, they are easily and predictably scalable; catering to larger datasets can be accommodated by increasing the number of filters or batch size and/or lowering the learning rates. Finally, they are easily modified for regression tasks e.g predicting subgrid wave or current fields from gridded weather variables (Sha et al., 2020), or estimating surf zone bathymetry (Collins et al., 2020).

A key aspect of Segmentation Gym is its link to an existing data labeling software, 'Doodler' (Buscombe et al., 2021). Labeled Earth science imagery can be rare and dataset

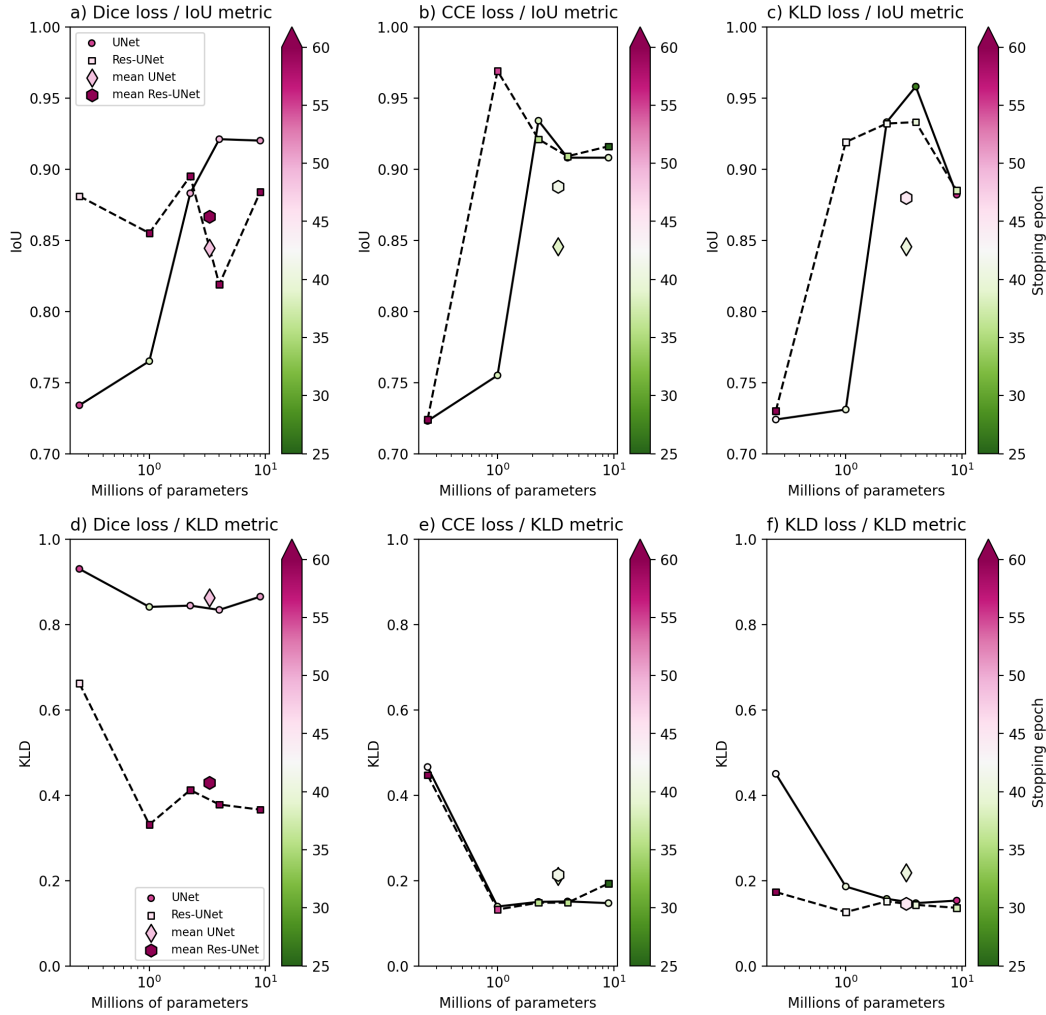


Figure 4. A summary of validation metrics for all 30 models. Each plot shows a model evaluation metric (mean IoU on the top row and KLD on the bottom) as a function of the number of model parameters. Dashed lines connecting square markers represent Res-UNets, and solid lines connecting circular markers represent UNets. Columns from left to right represent models trained using respectively Dice, CCE, and KLD for a loss function.

375 creation can be costly and it is not yet possible to know a priori how much data will be
 376 needed to train a segmentation model for a given task. Segmentation Gym is specifically
 377 designed to quickly and easily build models from Doodler output. This interoperabil-
 378 ity facilitates interactive data labeling and model building cycle, and permitting researchers
 379 to quickly evaluate whether they have enough labeled data to develop a model able to
 380 reach the desired level of a test metric.

381 The Segmentation Gym software can be used across a wide range of remotely sensed
 382 imagery, where there is a growing availability, size and relevancy of labeled datasets. Across
 383 Earth science fields, segmentation of aerial and satellite imagery is especially a common
 384 task (e.g. Vos et al., 2019; Bishop-Taylor et al., 2021). The software system we describe
 385 here allows for experimentation with many hyperparameters, and enables researchers to
 386 build and use performant models on any suitable dataset. We developed Segmentation
 387 Gym as an end-to-end reproducible workflow, whereby both labels and model results may
 388 be perfectly reproduced in another computing environment by an automated process.
 389 Donoho (2010) mentions several important advantages of computational reproducibil-
 390 ity, including improved transparency, improved continuity since others can build on the
 391 work, greater reusability that leads to greater impact, and obliging scientific funders that
 392 the work is preserved.

393 We envision future work can build from Segmentation Gym. For example, devel-
 394 oping a place to share models trained using Segmentation Gym, as well as relevant meta-
 395 data i.e., the configuration file, an example dataset, and a ‘model card’ for basic model
 396 inventory, reporting, and dissemination (Mitchell et al., 2019). Additionally, we provide
 397 a script to segment all images in a directory with a Gym model, but future work could
 398 expand this functionality so that models can be deployed in a range of settings (e.g., as
 399 a web or edge computing application, as an internal-facing research tool, etc.).

400 5 Open Source Statement

401 The Coast Train data used in this study are available from Wernette et al. (2022).
 402 The cross-platform open-source application ‘Segmentation Gym’ is available at [https://](https://github.com/Doodleverse/segmentation_gym)
 403 github.com/Doodleverse/segmentation_gym (Buscombe & Goldstein, 2022). Case study
 404 model weights and configuration files are available from Buscombe (2022a, 2022b).

405 Acknowledgments

406 This work has been supported by the U.S. Geological Survey Coastal/Marine Hazards
 407 and Resources Program and by Congressional appropriations through the Additional Sup-
 408 plemental Appropriations for Disaster Relief Act of 2019 (H.R. 2157). EBG acknowledges
 409 support from USGS (G20AC00403). The work described here began in preparation for
 410 ‘ML Mondays,’ an online course for application of deep-learning-based image analyses,
 411 supported by the U.S. Geological Survey Community of Data Integration. See [https://](https://dbuscombe-usgs.github.io/MLMONDAYS/)
 412 dbuscombe-usgs.github.io/MLMONDAYS/ for more information. Thanks to Leslie Hsu,
 413 Jon Warrick, Sharon Fitzpatrick, Chris Magirl, Kristen Splinter, Simon Topp, and an
 414 anonymous reviewer for valuable inputs. Any use of trade, firm, or product names is for
 415 descriptive purposes only and does not imply endorsement by the U.S. Government.

416 References

- 417 Abadi, M., Agarwal, A., Barham, P., Brevdo, E., Chen, Z., Citro, C., . . . Zheng, X.
 418 (2015). *TensorFlow: Large-scale machine learning on heterogeneous systems*.
 419 Retrieved from <https://www.tensorflow.org/>
 420 Bishop-Taylor, R., Nanson, R., Sagar, S., & Lymburner, L. (2021). Mapping Aus-
 421 tralia’s dynamic coastline at mean sea level using three decades of Landsat
 422 imagery. *Remote Sensing of Environment*, 267, 112734.

- 423 Buscombe, D. (2022a). Segmentation Zoo Res-UNet models for Landsat-8 satellite
424 imagery, Coast Train v1 Landsat-8 4-class subset [Software]. *Zenodo*. Retrieved
425 from <https://doi.org/10.5281/zenodo.6229071>
- 426 Buscombe, D. (2022b). Segmentation Zoo UNet models for Landsat-8 satellite im-
427 agery, Coast Train v1 Landsat-8 4-class subset [Software]. *Zenodo*. Retrieved
428 from <https://doi.org/10.5281/zenodo.6230083>
- 429 Buscombe, D., Goldstein, E., Sherwood, C., Bodine, C., Brown, J., Favela, J.,
430 ... Wernette, P. (2021). Human-in-the-Loop Segmentation of Earth Sur-
431 face Imagery. *Earth and Space Science*, e2021EA002085. Retrieved from
432 <https://doi.org/10.1029/2021EA002085>
- 433 Buscombe, D., & Goldstein, E. B. (2022). Segmentation Gym: Zenodo release for
434 journal article submission March 2022. [Software]. *Zenodo*. Retrieved from
435 <https://doi.org/10.5281/zenodo.6349591>
- 436 Buscombe, D., Wernette, P., Fitzpatrick, S., Favela, J., E.B., G., & Enwright,
437 N. (2022). A 1.2 Billion Pixel Human-Labeled Dataset for Data-Driven
438 Classification of Coastal Environments. *EarthArXiv*. Retrieved from
439 <https://doi.org/10.5066/P91NP87I>
- 440 Chen, Z., Liu, X., Yang, J., Little, E., & Zhou, Y. (2020). Deep learning-based
441 method for SEM image segmentation in mineral characterization, an example
442 from Duvernay Shale samples in Western Canada Sedimentary Basin. *Comput-
443 ers & Geosciences*, 138, 104450.
- 444 Chollet, F. (2021). *Deep learning with python*. Simon and Schuster.
- 445 Chollet, F., et al. (2015). *Keras*. <https://keras.io>.
- 446 Collins, A. M., Brodie, K. L., Spicer, B. A., Hesser, T. J., Farthing, M. W., Lee, J.,
447 & Long, J. W. (2020). Bathymetric inversion and uncertainty estimation from
448 synthetic surf-zone imagery with machine learning. *Remote Sensing*, 12(20),
449 3364.
- 450 *Conda*. (2022). Continuum Analytics, Inc. Retrieved from [https://docs.conda.io/
451 projects/conda/en/latest/](https://docs.conda.io/projects/conda/en/latest/)
- 452 Csurka, G., Larlus, D., Perronnin, F., & Meylan, F. (2004). What is a good evalua-
453 tion measure for semantic segmentation. *IEEE PAMI*, 26(1), 1–11.
- 454 Donoho, D. L. (2010). An invitation to reproducible computational research. *Bio-
455 statistics*, 11(3), 385–388.
- 456 Drozdal, M., Vorontsov, E., Chartrand, G., Kadoury, S., & Pal, C. (2016). The im-
457 portance of skip connections in biomedical image segmentation. In *Deep learn-
458 ing and Data Labeling for Medical Applications* (pp. 179–187). Springer.
- 459 Gil, Y., David, C. H., Demir, I., Essawy, B. T., Fulweiler, R. W., Goodall, J. L., ...
460 Oh, J.-H. (2016). Toward the Geoscience paper of the future: Best practices
461 for documenting and sharing research from data to software to provenance.
462 *Earth and Space Science*, 3(10), 388–415.
- 463 Gupta, A., Watson, S., & Yin, H. (2021). Deep learning-based aerial image segmen-
464 tation with open data for disaster impact assessment. *Neurocomputing*, 439,
465 22–33.
- 466 Harris, C. R., Millman, K. J., van der Walt, S. J., Gommers, R., Virtanen, P., Cour-
467 napeau, D., ... Oliphant, T. E. (2020). Array programming with NumPy.
468 *Nature*, 585(7825), 357–362. doi: 10.1038/s41586-020-2649-2
- 469 Hoerer, T., & Kuenzer, C. (2020). Object detection and image segmentation with
470 deep learning on Earth observation data: A review. Part I: Evolution and
471 recent trends. *Remote Sensing*, 12(10), 1667.
- 472 Jin, C., Wang, K., Han, T., Lu, Y., Liu, A., & Liu, D. (2022). Segmentation of ore
473 and waste rocks in borehole images using the multi-module densely connected
474 u-net. *Computers & Geosciences*, 159, 105018.
- 475 Kattenborn, T., Eichel, J., & Fassnacht, F. E. (2019). Convolutional Neural Net-
476 works enable efficient, accurate and fine-grained segmentation of plant species
477 and communities from high-resolution UAV imagery. *Scientific Reports*, 9(1),

- 478 1–9.
- 479 Kingma, D. P., & Ba, J. (2014). Adam: A method for stochastic optimization. *arXiv*
- 480 *preprint arXiv:1412.6980*.
- 481 Kotaridis, I., & Lazaridou, M. (2021). Remote sensing image segmentation ad-
- 482 vances: A meta-analysis. *ISPRS Journal of Photogrammetry and Remote Sens-*
- 483 *ing, 173*, 309–322.
- 484 LeCun, Y., Bengio, Y., & Hinton, G. (2015). Deep learning. *Nature, 521*(7553),
- 485 436–444.
- 486 Li, S., Liu, N., Li, F., Gao, J., & Ding, J. (2022). Automatic fault delineation in 3d
- 487 seismic images with deep learning: Data augmentation or ensemble learning?
- 488 *IEEE Transactions on Geoscience and Remote Sensing*.
- 489 Liu, C.-C., Zhang, Y.-C., Chen, P.-Y., Lai, C.-C., Chen, Y.-H., Cheng, J.-H., & Ko,
- 490 M.-H. (2019). Clouds classification from Sentinel-2 imagery with deep residual
- 491 learning and semantic image segmentation. *Remote Sensing, 11*(2), 119.
- 492 Luijendijk, A., Hagenaars, G., Ranasinghe, R., Baart, F., Donchyts, G., &
- 493 Aarninkhof, S. (2018). The state of the world’s beaches. *Scientific Reports,*
- 494 *8*(1), 1–11.
- 495 Marangio, P., Christodoulou, V., Filgueira, R., Rogers, H. F., & Beggan, C. D.
- 496 (2020). Automatic detection of Ionospheric Alfvén Resonances in magnetic
- 497 spectrograms using U-net. *Computers & Geosciences, 145*, 104598.
- 498 Mitchell, M., Wu, S., Zaldivar, A., Barnes, P., Vasserman, L., Hutchinson, B., ...
- 499 Gebu, T. (2019). Model cards for model reporting. In *Proceedings of the*
- 500 *Conference on Fairness, Accountability, and Transparency* (pp. 220–229).
- 501 Nagi, A. S., Kumar, D., Sola, D., & Scott, K. A. (2021). RUF: Effective Sea Ice
- 502 Floe Segmentation Using End-to-End RES-UNET-CRF with Dual Loss. *Re-*
- 503 *remote Sensing, 13*(13), 2460.
- 504 Nalepa, J., Myller, M., & Kawulok, M. (2019). Validating hyperspectral image seg-
- 505 mentation. *IEEE Geoscience and Remote Sensing Letters, 16*(8), 1264–1268.
- 506 Ostblom, J., & Timbers, T. (2021). Opinionated practices for teaching repro-
- 507 ducibility: motivation, guided instruction and practice. *arXiv preprint*
- 508 *arXiv:2109.13656*.
- 509 Pally, R., & Samadi, S. (2022). Application of image processing and convolutional
- 510 neural networks for flood image classification and semantic segmentation. *En-*
- 511 *vironmental Modelling & Software, 148*, 105285.
- 512 Parker, H. (2017). Opinionated analysis development. *PeerJ Preprints, 5*, e3210v1.
- 513 Peng, R. D., & Parker, H. S. (2021). Perspective on data science. *Annual Review of*
- 514 *Statistics and Its Application, 9*.
- 515 Rafique, M. U., Zhu, J., & Jacobs, N. (2022). Automatic segmentation of sink-
- 516 holes using a convolutional neural network. *Earth and Space Science, 9*(2),
- 517 e2021EA002195.
- 518 Ronneberger, O., Fischer, P., & Brox, T. (2015). U-net: Convolutional networks for
- 519 biomedical image segmentation. In *International Conference on Medical Image*
- 520 *Computing and Computer-Assisted Intervention* (pp. 234–241).
- 521 Sáez, F. J., Catalan, P. A., & Valle, C. (2021). Wave-by-wave nearshore wave break-
- 522 ing identification using U-Net. *Coastal Engineering, 170*, 104021.
- 523 Schmidt, R. M., Schneider, F., & Hennig, P. (2020). Descending through a
- 524 crowded valley: Benchmarking deep learning optimizers. *arXiv preprint*
- 525 *arXiv:2007.01547*.
- 526 Sha, Y., Gagne II, D. J., West, G., & Stull, R. (2020). Deep-learning-based grid-
- 527 ded downscaling of surface meteorological variables in complex terrain. Part I:
- 528 Daily maximum and minimum 2-m temperature. *Journal of Applied Meteorol-*
- 529 *ogy and Climatology, 59*(12), 2057–2073.
- 530 Song, Q., Cui, Z., & Liu, P. (2020). An efficient solution for semantic segmenta-
- 531 tion of three ground-based cloud datasets. *Earth and Space Science, 7*(4),
- 532 e2019EA001040.

- 533 Stivaktakis, R., Tsagkatakis, G., & Tsakalides, P. (2019). Deep learning for mul-
 534 tilabel land cover scene categorization using data augmentation. *IEEE Geo-*
 535 *science and Remote Sensing Letters*, 16(7), 1031–1035.
- 536 Sun, Z., Sandoval, L., Crystal-Ornelas, R., Mousavi, S. M., Wang, J., Lin, C., ...
 537 others (2022). A review of Earth Artificial Intelligence. *Computers & Geo-*
 538 *sciences*, 105034.
- 539 *Tensorflow datasets*. (2022). Retrieved from [https://www.tensorflow.org/guide/](https://www.tensorflow.org/guide/data)
 540 [data](https://www.tensorflow.org/guide/data)
- 541 van der Meij, W. M., Meijles, E. W., Marcos, D., Harkema, T. T., Candel, J. H., &
 542 Maas, G. J. (2021). Comparing geomorphological maps made manually and by
 543 deep learning. *Earth Surface Processes and Landforms*, 47(4), 1089 - 1107.
- 544 van Lieshout, C., van Oeveren, K., van Emmerik, T., & Postma, E. (2020). Au-
 545 tomated river plastic monitoring using deep learning and cameras. *Earth and*
 546 *Space Science*, 7(8), e2019EA000960.
- 547 Verma, U., Chauhan, A., MM, M. P., & Pai, R. (2021). Deeprivwidth: Deep learn-
 548 ing based semantic segmentation approach for river identification and width
 549 measurement in sar images of coastal karnataka. *Computers & Geosciences*,
 550 154, 104805.
- 551 Vos, K., Splinter, K. D., Harley, M. D., Simmons, J. A., & Turner, I. L. (2019).
 552 CoastSat: A Google Earth Engine-enabled Python toolkit to extract shorelines
 553 from publicly available satellite imagery. *Environmental Modelling & Software*,
 554 122, 104528.
- 555 Wernette, P., Buscombe, D., Favela, J., Fitzpatrick, S., & EB, G. (2022). Coast
 556 Train–Labeled imagery for training and evaluation of data-driven models for
 557 image segmentation [Dataset]. *U.S. Geological Survey Data Release*. Retrieved
 558 from <https://doi.org/10.5066/P91NP87I>
- 559 Xiao, H., Zhang, F., Shen, Z., Wu, K., & Zhang, J. (2021). Classification of weather
 560 phenomenon from images by using deep convolutional neural network. *Earth*
 561 *and Space Science*, 8(5), e2020EA001604.
- 562 Yuan, X., Shi, J., & Gu, L. (2021). A review of deep learning methods for seman-
 563 tic segmentation of remote sensing imagery. *Expert Systems with Applications*,
 564 169, 114417.
- 565 Zhang, Z., Liu, Q., & Wang, Y. (2018). Road extraction by deep residual U-Net.
 566 *IEEE Geoscience and Remote Sensing Letters*, 15(5), 749–753.